Catal Lett (2011) 141:633–640
DOI 10.1007/s10562-011-0565-7

Surface Composition and Catalytic Evolution of Au_xPd_{1-x} (x = 0.25, 0.50 and 0.75) Nanoparticles Under CO/O_2 Reaction in Torr Pressure Regime and at 200 °C

Selim Alayoglu · Franklin Tao · Virginia Altoe · Colin Specht · Zhongwei Zhu · Funda Aksoy · Derek R. Butcher · Russ J. Renzas · Zhi Liu · Gabor A. Somorjai

Received: 3 December 2010 / Accepted: 10 February 2011 / Published online: 8 March 2011

Abstract Au_xPd_{1-x} (x = 0, 0.25, 0.5, 0.75, 1) nanoparticle (NP) catalysts (8–11 nm) were synthesized by a one-pot reaction strategy using colloidal chemistry. XPS depth profiles with variable X-ray energies and scanning transmission electron microscopy (STEM) analyses show that the as-synthesized Au_xPd_{1-x} (x = 0.25 and 0.5) bimetallic NPs have gradient alloy structures with Au-rich cores and Pd-rich shells. The evolution of composition and structure in the surface region corresponding to a mean free path of 0.6–0.8 nm (i.e., 2–3 layers to the bulk from the particle surface) was studied with ambient pressure X-ray photoelectron spectroscopy (AP-XPS) under CO/O_2 reaction in the Torr pressure regime. Under the reaction conditions of 80 mTorr CO and 200 mTorr O_2 at 200 °C, the surface region of $Au_{0.75}Pd_{0.25}$ NP is Au-rich (~70% by Au). All Au_xPd_{1-x} (x = 0.25, 0.5, 0.75) NP catalysts have higher turnover rates for the model CO/O_2 reaction than pure Pd and pure Au NPs. The Pd-rich $Au_{0.25}Pd_{0.75}$ NPs show the highest turnover rates and the Pd-rich $Au_{0.5}Pd_{0.5}$ NPs the lowest turnover rates at 200 °C. Interestingly, the Au-rich $Au_{0.75}Pd_{0.25}$ NPs exhibit steady-state turnover rates which are intermediate to those of the Pd-rich bimetallic nanoparticles.

Keywords Nanoparticles · Gold · Palladium · Ambient pressure X-ray photoelectron spectroscopy · CO/O_2 reaction · Surface composition

Selim Alayoglu and Franklin Tao contributed equally to this work.

Electronic supplementary material The online version of this article (doi:10.1007/s10562-011-0565-7) contains supplementary material, which is available to authorized users.

S. Alayoglu · F. Tao · C. Specht · Z. Zhu · D. R. Butcher · R. J. Renzas · G. A. Somorjai (✉)
Department of Chemistry, University of California, Berkeley, CA 94720, USA
e-mail: somorjai@berkeley.edu

S. Alayoglu · F. Tao · C. Specht · Z. Zhu · D. R. Butcher · R. J. Renzas
Materials Science Division, Lawrence Berkeley National Laboratory, Berkeley, CA 94720, USA

V. Altoe
Molecular Foundry, Lawrence Berkeley National Laboratory, Berkeley, CA 94720, USA

F. Aksoy · Z. Liu
Advanced Light Sources, Lawrence Berkeley National Laboratory, Berkeley, CA 94720, USA

Present Address:
F. Tao
Department of Chemistry and Biochemistry, University of Notre Dame, Notre Dame, IN 46556, USA

1 Introduction

Alloying metal catalysts can tune the electronic structure of metals through geometric or/and ligand effects on the surface, potentially increasing catalytic activity and enhancing selectivity [1–9]. Bimetallic catalysts are used in numerous reactions, including catalytic reforming [7, 10–12], combustion, [13, 14] and alcohol oxidation [15]. In many cases, they present superior catalytic activity and selectivity than single-component metal catalysts [5, 6]. An early series of bimetallic catalysts developed by Sinfelt is Group IB-VIII bimetallic catalysts in 1980s. The addition of Group IB metal (Cu, Ag, or Au) into Group VIII metal (Ru, Co, or Ni) inhibits hydrogenolysis of hydrocarbons and therefore improves selectivity in aromatization and isomerization of hydrocarbons [16]. However, mechanistic

understanding of the factors of electronic and geometric structures at atomic level is still lacking due to the absence of in situ information about surface structure and composition under reaction conditions.

Here we selected Au_xPd_{1-x} bimetallic nanoparticle system as model catalysts [4, 17–24]. CO/O_2 reaction was chosen to avoid different products of parallel reaction channels so that we could have a better understanding of relationship of surface composition and catalytic activity. We synthesized size- and composition-controlled bimetallic Au_xPd_{1-x} ($x = 0$, 0.25, 0.5, 0.75, 1.0) NPs with narrow size distributions about 8–11 nm employing a modified colloidal synthesis method. Then, we characterized these nanoparticle catalysts on the surface and in the bulk employing various techniques such as transmission electron microscopy (TEM), scanning transmission electron microscopy with energy dispersive spectroscopy (STEM/EDS), X-ray diffraction (XRD), UV/vis spectroscopy and X-ray photoelectron spectroscopy (XPS). Finally, we carried out reaction studies to evaluate both catalytic and structural evolution of these well-defined nanoparticle catalysts in batch reactor systems under identical pressure and temperature conditions. We explored how the reaction rates depend on the particle size and surface composition of the monodisperse Au_xPd_{1-x} ($x = 0$, 0.25, 0.5, 0.75, 1.0) NPs for the model CO/O_2 reaction. We found that the bimetallic Au_xPd_{1-x} ($x = 0.25$ and 0.5) NPs formed with Au-rich cores and Pd-rich shells. The $Au_{0.25}Pd_{0.75}$ and $Au_{0.5}Pd_{0.5}$ NPs maintained their surface compositions (i.e., particle architectures) under the CO/O_2 reaction in the Torr pressure regime and at 200 °C. For the $Au_{0.75}Pd_{0.25}$ NPs, surface enrichment of Au was detected at 200 °C (i.e., nanoparticles with Au-rich shells). For the reaction mixture of 80 mTorr CO and 200 mTorr O_2 at 200 °C, the catalytic evaluation of the monometallic and bimetallic NP catalysts revealed that all the bimetallic nanoparticle catalysts are catalytically more active than pure Au and pure Pd NPs.

2 Experimental

The Au_xPd_{1-x} nanoparticles ($x = 0$, 0.25, 0.5, 0.75, 1) were synthesized in a one-step process that involves the reduction of two precursors under Ar gas, using poly(vinylpyrrolidone) (PVP) as a surfactant. To synthesize Au_xPd_{1-x} nanoparticles, $HAuCl_4$ and $(NH_4)_2PdCl_4$ with specific atomic ratios and PVP were added to 1,4-butanediol in a 50 ml three-necked flask at room temperature. For example, in the synthesis of $Au_{0.25}Pd_{0.75}$ nanoparticles, 8.9 mg $HAuCl_4$ precursor salt and 19.0 mg $(NH_4)_2PdCl_4$ precursor salt were dissolved in 10 mL 1,4-butanediol in the presence of 55 mg polyvinylpyrolidone (PVP) as capping agent in a 50 mL 3-neck round bottom flask. The stock solution was heated to 80 °C and the flask was evacuated for 15 min, and then flushed with Ar at this temperature. Pumping and purging cycles were repeated for three times. Then, the yellow solution was heated from 80–230 °C with a ramping rate of 10 °C per minute. Solution turned black and became colloidal within 2 min under refluxing solvent at 225 °C. The reaction was left to reflux for 30 min. The colloidal suspension of nanoparticles was diluted to 50 mL by acetone and centrifuged at 4000 rpm for 10 min. Nanoparticles were washed with acetone and re-dispersed in 20% by volume ethanol chloroform mixtures to a final concentration of 10 mM for characterization and preparation of Langmuir–Blodgett (LB) films. Syntheses of the other bimetallic Au_xPd_{1-x} ($x = 0.5$, 0.75) NPs are the same as described above except different amount of the precursor salts used to follow the nominal composition and a total concentration of 10 mM. The precipitated Au_xPd_{1-x} nanoparticles were washed with acetone and then re-dispersed in ethanol. To synthesize ca. 8 nm Au NPs, 30 mL ethylene glycol (EG) containing 33.4 mg $HAuCl_4$ and 28.0 mg PVP_{55k} was brought to 60 °C in an oil bath. To this reaction mixture, 5 mL of 0.05 M $NaBH_4$ solution in EG was rapidly injected. The reaction flask was covered with aluminum foil and the solution left to stir for 12 h at 60 °C. The purple colloidal suspension was centrifuged, washed and re-dispersed in ethanol–chloroform mixture as described above. The shape, size, and crystallinity of the nanoparticles were examined by high resolution TEM (Jeol 2100F, 200 kV and Philips CM300, 300 kV) and X-ray diffraction (XRD, Bruker D8 GADDS, Co–K_α radiation of $\lambda = 1.79$ Å).

Sub-monolayers of bimetallic nanoparticle catalysts on silicon wafers were prepared by placing certain amount of nanoparticle colloidal suspension onto the water subphase of a Langmuir–Blodgett (LB) trough (Nima Technology, M611) at room temperature. The resulting layer was compressed at a rate of 5 cm^2/min and transferred onto a silicon wafer using the Langmuir–Schäffer horizontal lift-off method. The nanoparticle films on the silicon wafers were examined with scanning electron microscopy (Zeiss Ultra55). X-ray photoemission features of Au 4f, Pd 3d, Si 2p, and C 1s core levels were studied using synchrotron-based XPS and a lab-based XPS with Al Kα X-ray source. The peak intensities used to determine the atomic fractions of the two elements were calibrated using the photo-ionization cross sections corresponding to the X-ray energies.

Typically, micro-reactor in line with gas chromotograph (GC) is used to measure activity of catalysts under ambient pressure conditions. However, the highest pressure of reactants in the reaction cell of AP-XPS is limited to 1–2 Torr for technical limitations. In order to avoid the potential pressure gap, a low-pressure batch reactor working within the range of 0.1–760 Torr and 25–300 °C was

built. To identify the potential impact of the restructured surface composition on the model CO/O_2 reaction, catalytic measurements were performed under identical reaction conditions of the AP-XPS studies. Reactants can be introduced using leak valves while closely monitoring the pressure of the reaction chamber, and the products have been monitored online using quadrupole mass spectrometer. The surface area and the number of surface metal sites have been calculated from the TEM-projected surface area of the nanoparticles (the average surface area of each nanoparticle), the coverage of the nanoparticles in fractions of a monolayer (sub-monolayer on silicon layer), the geometric area of Si substrate, and the surface packing density of the metals. In order to calculate the total surface area of the nanoparticles at monolayer coverage, the results from the XPS analyses of Si2p, Au4f and Pd3d core levels and the number densities (per area) from the SEM particle histograms have been used separately, and are in good agreement. For the calculation of the surface metal sites, the total surface area at monolayer coverage was divided by the surface packing density derived from the (surface) composition-averaged atomic distances of pure metals (although the derivation of such relation took into account the surface as well as volume densities). XRD patterns of monometallic nanoparticles were refined to extract the atomic distances of pure metals. Given the comparable (and relatively low) turnover rates measured over the monometallic Au and Pd NPs, no discrimination was made between Au and Pd as to the actual identity of the catalytically active surface sites in the case of the bimetallic Au–Pd NPs.

3 Results

Composition-controlled bimetallic Au_xPd_{1-x} ($x = 0$, 0.25, 0.5, 0.75, 1.0) nanoparticles were synthesized employing a modified polyol reduction protocol. $HAuCl_4$ and $(NH_4)_2PdCl_4$ precursor salt mixtures are usually reduced and nucleated in the presence of PVP at the boiling temperature of 1,4-butanediol. The *initial* nucleates present colors similar to colloidal Au NPs (purple). When the reactions are complete, the colloidal $Au_{0.25}Pd_{0.75}$ and $Au_{0.5}Pd_{0.5}$ NPs are black. Notably, the as-synthesized Au-rich $Au_{0.75}Pd_{0.25}$ NPs have discernible dark purple colors. Monometallic Pd NPs synthesized under similar reaction conditions are 9.5 nm in average. Monometallic Au NPs can not be obtained under similar reaction conditions. Hence, 8 nm PVP-capped Au NPs were prepared in EG via $NaBH_4$ reduction.

Average particle sizes increase with nominal composition of Au precursor from 8.1 ± 2.3 nm for the Pd-rich $Au_{0.25}Pd_{0.75}$ to 11.0 ± 2.9 nm for the Au-rich $Au_{0.75}Pd_{0.25}$. Figure 1 presents TEM images and particle size histograms

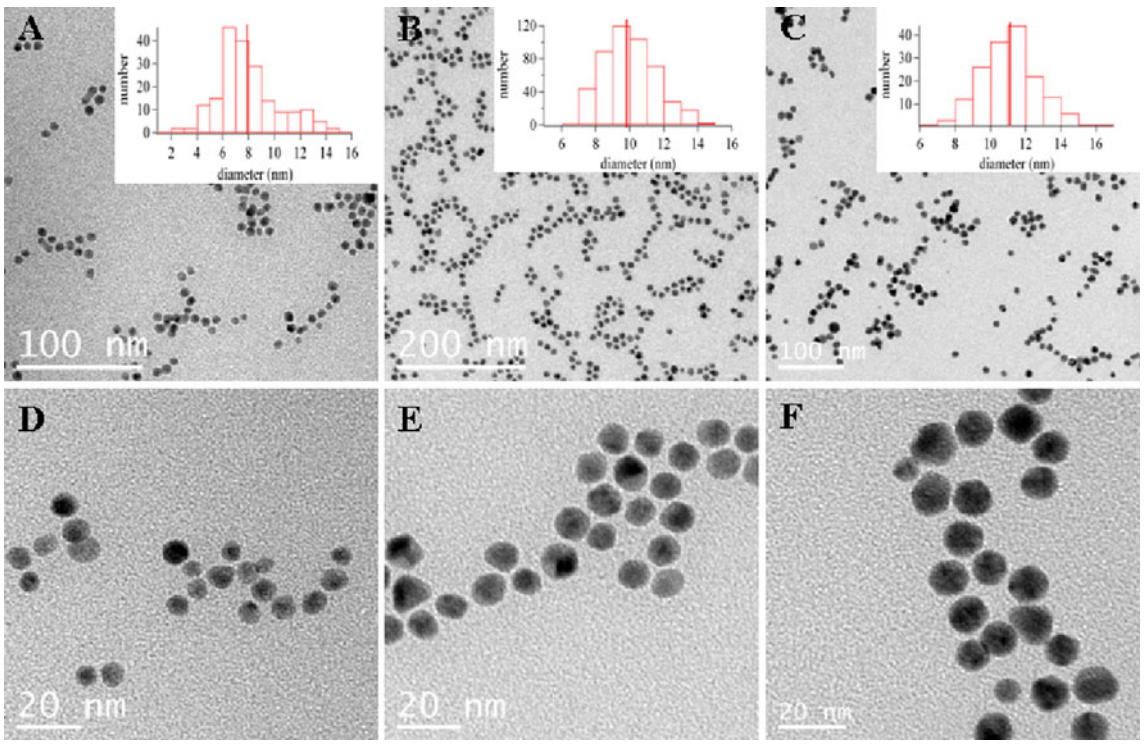

Fig. 1 TEM images and particle size histograms of $Au_{0.25}Pd_{0.75}$ (**a**, **d**), $Au_{0.5}Pd_{0.5}$ (**b**, **e**), and $Au_{0.75}Pd_{0.25}$ (**c**, **f**). *Scale bars* are given in each picture

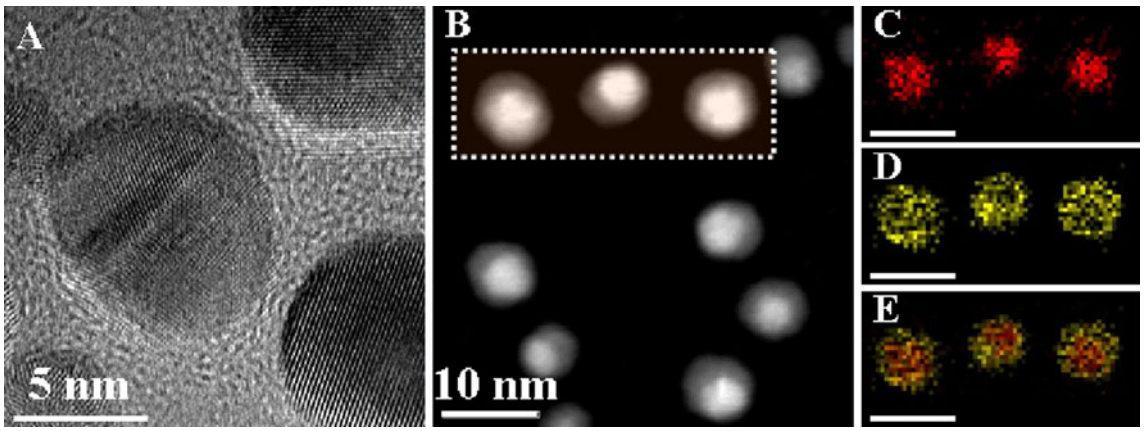

Fig. 2 HR-TEM and HAADF images of $Au_{0.25}Pd_{0.75}$ NPs (**a** and **b**, respectively). Representative STEM-EDS phase maps, showing Au K line (**c**), Pd L line (**d**) and Au K and Pd L lines combined (**e**). *Scale bars* are 10 nm in **b**–**e**

of the Au_xPd_{1-x} ($x = 0.25, 0.5, 0.75$) NPs. Figure 2 shows the representative high angle annular dark field (HAADF), high resolution transition electron microscopy (HR-TEM) images, and STEM/EDS mapping configuration of Pd-rich $Au_{0.25}Pd_{0.75}$ nanoparticles. In fact, all the bimetallic Au_xPd_{1-x} NPs described in this study exhibit Au-rich core/Pd-rich shell type gradient alloy evidenced in their EDS mapping configuration (Fig. 2). Figure S4 show the model clusters derived from the starting metal compositions, basic geometric constraints and experimental STEM/EDS phase maps of the Au_xPd_{1-x} ($x = 0.25, 0.5, 0.75$) NPs. Based on the EDS spectra of multiple single nanoparticles, the average atomic fraction of Pd in each Au_xPd_{1-x} NPs is calculated to be 0.76 ± 0.06 for the $Au_{0.25}Pd_{0.75}$ NPs and 0.24 ± 0.05 for the $Au_{0.75}Pd_{0.25}$ NPs, is consistent with the starting compositions of the metal precursor salts.

The crystallinity of Au_xPd_{1-x} ($x = 0, 0.25, 0.5, 0.75, 1$) NPs were confirmed by XRD studies (Fig. 3). NaCl salt was used as internal standard to determine the XRD patterns of the bimetallic nanoparticles normalized with respect to the diffraction geometry. Single FCC pattern for all the bimetallic Au_xPd_{1-x}NPs can be clearly identified, confirming well crystallization during synthesis. Notably, the XRD patterns of Au_xPd_{1-x} NPs are shifted to higher 2-theta compared to the monometallic Pd NPs. In addition, the amount of the shifts of the diffraction pattern depends on the composition of nanoparticles as expected by the Vegard's law.

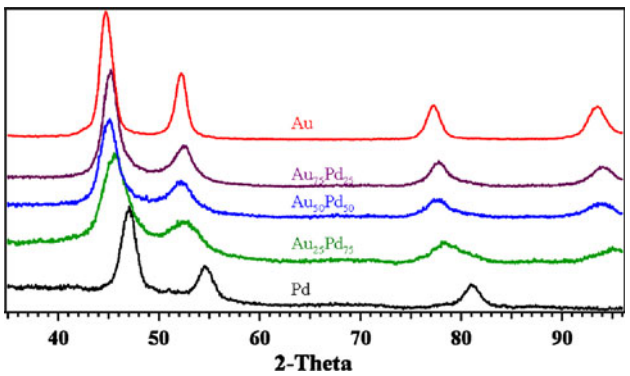

Fig. 3 XRD patterns of $Au_{1-x}Pd_x$ ($x = 0$–1) NPs with increasing % Pd from *top* to *bottom*

UV/vis spectra of the monometallic Pd and Pd-rich $Au_{0.25}Pd_{0.75}$ NPs do not have a surface plasmon resonance (SPR) band in the visible region (see supporting information: Fig. S1). However, clear SPR bands at 530 nm were observed in the UV/vis spectra of Au_xPd_{1-x} ($x = 0.5$, 0.75). The difference in the SPR band between $Au_{0.25}Pd_{0.75}$ and $Au_{0.75}Pd_{0.25}$ is in good agreement with the observed colors of NPs colloids upon synthesis.

Surface composition of the as-synthesized Au_xPd_{1-x} NPs dispersed on silicon wafers was measured by synchrotron-based XPS and conventional XPS under vacuum condition. The SEM images of the sub-monolayer of 2-D nanoparticles catalysts are shown in the supporting information. The PVP capping was removed by outgassing the samples at 100 °C in high vacuum and a subsequent annealing to 100–150 °C in low pressure of oxygen (1×10^{-5} Torr) before the XPS studies. As shown in Fig. S2, this pretreatment removed the majority of PVP as suggested by the change in the relative intensity of the C1s, N1s and the substrate Si 2p peaks [25]. X-rays with energy of 380, 450, and 1486.6 eV were used to excite Au 4f electrons. Corresponding to these X-rays, the kinetic energy of the measured photoelectrons are ~300, ~380, and ~1400 eV. Electrons on Pd 3d core level were excited by using X-rays with energies of 650, 730, and 1486.6 eV. Figure 4 shows the measured atomic fractions of Au and Pd as a function of kinetic energy of photoelectron and the corresponding mean free paths. Obviously, the atomic

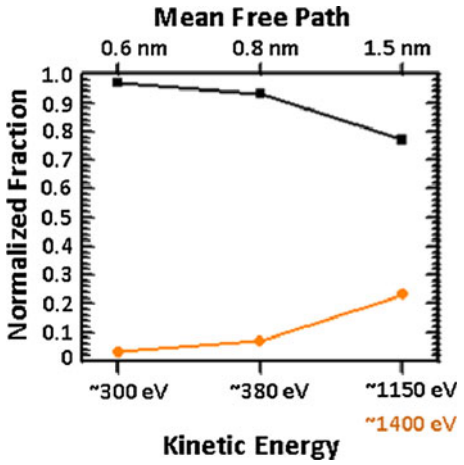

Fig. 4 Normalized Pd (*black*) and Au (*gold*) fractions are plotted versus kinetic energy of X-rays from depth-probed XPS analysis for $Au_{0.25}Pd_{0.75}$

fraction of Pd in surface region ($\sim$3 layer thick) of $Au_{0.25}Pd_{0.75}$ is nearly 100%, and drops down to the nominal (i.e., bulk) composition (75% Pd) in the volume corresponding to a mean free path of 1.5 nm. In the surface region ($\lambda = 0.6$ nm), atom fractions of Pd are $\sim$95% in $Au_{0.5}Pd_{0.5}$ and $\sim$80% in $Au_{0.75}Pd_{0.25}$. Atom fractions of Pd in the equi-molar and Au-rich samples never reach the nominal (i.e., bulk) composition. These samples always remain Pd-rich in the surface regions as probed by the XPS.

The Au_xPd_{1-x} ($x = 0$, 0.25, 0.5, 0.75, 1) NPs on silicon substrates were then studied using AP-XPS. Figure 5 presents the atomic fractions of $Au_{0.25}Pd_{0.75}$, $Au_{0.5}Pd_{0.5}$, and $Au_{0.75}Pd_{0.25}$ NPs under vacuum and various gas atmospheres. The XPS spectra of Au4f and Pd3d core levels were continuously recorded (i.e., ca. 60 min for the CO/O_2 reaction conditions, and ca 30 min for the other vacuum and reactive gas conditions) until no discernible spectral changes could be observed. Prior to the XPS screening, the samples were preconditioned at 100 °C and under vacuum for several hours to remove the PVP capping. This pretreatment does not induce any significant structural and chemical perturbation to the nanoparticles, and thus are quite effective in removing the majority of PVP capping (vide infra) [25]. During the XPS screening, the surface composition remained unchanged for the $Au_{0.25}Pd_{0.75}$ and $Au_{0.5}Pd_{0.5}$ NPs under vacuum, reactive gas atmospheres (H_2, CO, O_2 etc.) and CO/O_2 reaction. For the $Au_{75}Pd_{25}$ NPs, on the other hand, the topmost surface layers have been transformed from the 80% Pd-rich state to 65% Au-rich state at 200 °C. Control experiments revealed the detailed structural and chemical evolution of the $Au_{75}Pd_{25}$ NPs: (1) No significant change in the surface composition was observed in vacuum, neither H_2 nor CO atmospheres. (2) Pd is ca. 80% metallic (i.e., 20% PdO_x) under vacuum, H_2 and CO atmospheres at 200 °C. (3) CO/O_2 reaction gas mixture (i.e., 80 mTorr CO and 200 mTorr O_2) resulted in significant Au segregation to the surface at 200 °C, which reached the equilibrium composition in ca. 30 min. (4) The chemical composition of Pd drops to ca. 65% metallic (i.e., 35% PdO_x) under O_2-rich CO/O_2 reaction at 200 °C. (5) The changes in surface composition are irreversible and the Au-rich surface state remains stable in vacuum. Notably, there is no significant Au segregation observed in surface regions of $Au_{0.25}Pd_{0.75}$ and $Au_{0.5}Pd_{0.5}$ even under CO/O_2 gas mixture at 200 °C (Fig. 4a, b).

A homebuilt low pressure reactor was used for the measurement of catalytic activity under the CO oxidation reaction conditions on the Au–Pd nanoparticles under conditions similar to those used in our AP-XPS studies. The turnover rates are shown in Fig. 6 for the Au_xPd_{1-x}

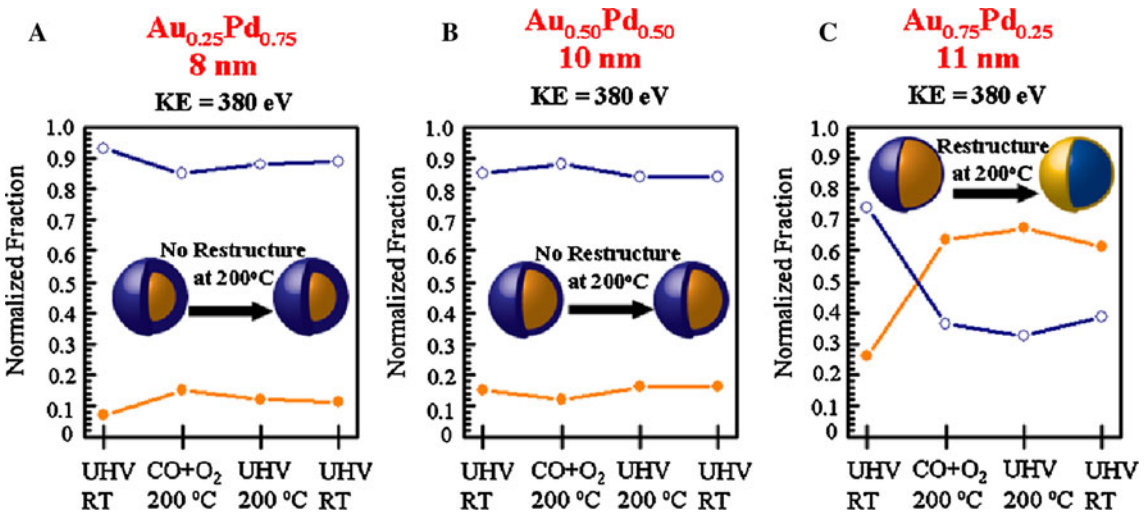

Fig. 5 Normalized Pd (*blue*) and Au (*gold*) fractions are plotted versus various temperatures and pressure (i.e., CO oxidation reaction) conditions from ambient pressure XPS analysis using 380 eV X-rays for $Au_{0.25}Pd_{0.75}$ (**a**), $Au_{0.5}Pd_{0.5}$ (**b**) and $Au_{0.75}Pd_{0.25}$ (**c**)

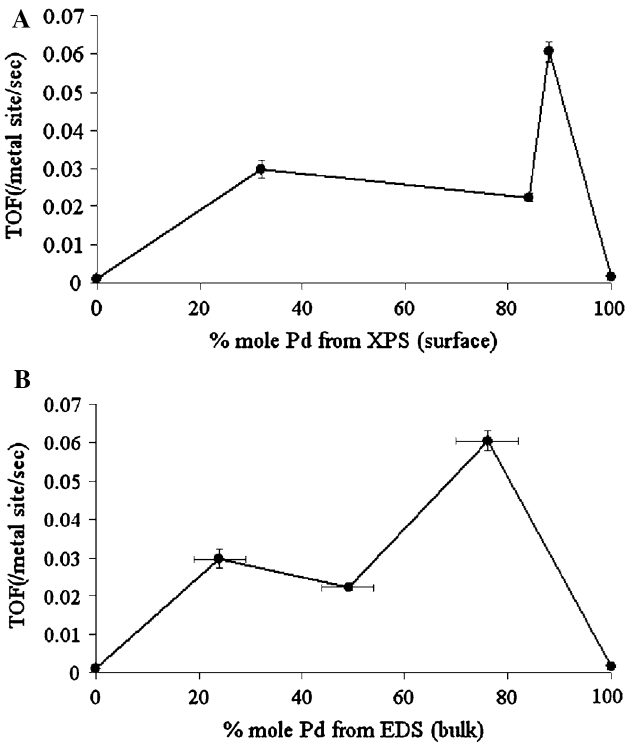

Fig. 6 A plot of the turnover rates in CO molecules/metal site/sec at 200 °C versus % atom by Pd measured by AP-XPS using 300 eV photoelectrons (**a**) and EDS (**b**)

($x = 0$–1) NPs at 200 °C. Turnover frequency (TOF) in CO molecules consumed per metal site per second is plotted in the y-axis, and % concentration by Pd as measured by AP-XPS using 300 eV photoelectrons (Fig. 6a) and EDS (Fig. 6b) in the x-axis. Based on our analysis, all the bimetallic Au–Pd nanoparticle catalysts studied outperform the monometallic Au and Pd catalysts of comparable average sizes. At 200 °C, the Pd-rich $Au_{0.25}Pd_{0.75}$ NPs show the highest turnover rates among all the bimetallic catalysts studied. Second to the $Au_{0.25}Pd_{0.75}$ NPs, the Au-rich $Au_{0.75}Pd_{0.25}$ NPs are slightly more active than the Pd-rich $Au_{0.5}Pd_{0.5}$ NPs in the steady-state. An interesting finding of this study is that the Au-rich $Au_{0.75}Pd_{0.25}$ NPs outperforms in catalytic activity in the CO/O_2 reaction at 200 °C. Also note that our AP-XPS studies revealed the intra-particle restructuring for the $Au_{0.75}Pd_{0.25}$ NPs under identical temperature and pressure conditions. Differently, the Pd-rich $Au_{0.25}Pd_{0.75}$ and $Au_{0.5}Pd_{0.5}$ NPs maintain their surface chemical and compositional make-up under identical conditions. For the $Au_{0.25}Pd_{0.75}$ and $Au_{050}Pd_{0.50}$ samples, there was no time dependence of the turnovers rates. However, the $Au_{0.75}Pd_{0.25}$ sample showed time dependence on the catalytic turnovers at 200 °C. More studies are needed for exploring this phenomenon in the future.

Notably, SEM studies show that there is no post-catalysis aggregation or sintering of NPs for the Au–Pd system even after the reaction at 250 °C (Fig. S3). Additionally, our AP-XPS studies revealed no significant changes in the surface composition for the Pd-rich $Au_{0.25}Pd_{0.75}$ and $Au_{0.5}Pd_{0.5}$ NPs measured at 200 °C. Similarly, the $Au_{0.75}Pd_{0.25}$ NPs exhibit a certain Au-rich surface state under temperature and pressure conditions of the CO/O_2 reaction at 200 °C.

4 Discussion

4.1 Formation of Au_xPd_{1-x} ($x = 0.25, 0.5, 0.75$) with Pd-Rich Surface Region

We have employed a modified polyol reduction reaction method using 1,4-butandiol as the reducing solvent and PVP as the capping agent [26–29]. As investigated in vacuum at ambient temperature by synchrotron XPS, the topmost surface layers mainly consist of Pd atoms. The UV–Vis spectra and the appearance of purple colloidal color at the early stages of nucleation suggest the preferential formation of Au-rich cores. Consistent with the reported literature, we have found that the present synthetic route leads to all bimetallic nanoparticles (Au_xPd_{1-x}, $x = 0.25, 0.5, 0.75$) with Pd-rich shells for the entire composition series studied.

Table 1 shows some physical and chemical properties of Pd and Au, including cohesive energy and surface free energies per atom, and adsorption energies per moles of CO or O_2 adsorbed. Lower surface free energy of Au (1.63 J/m^2 or 0.85 eV/atom) relative to Pd (2.05 J/m^2 or 0.97 eV/atom) and larger cohesive energy of Pd (3.86 eV/atom) relative to Au (3.81 eV/atom) would lead to the formation of Au_xPd_{1-x} NPs with Au-rich surfaces [30, 31]. O_2 and/or CO adsorption, however, stabilizes nanoparticles

Table 1 Some physical and chemical properties of Pd and Au (111) single crystal surfaces

Atom	Cohesive energy[a] (eV/atom)	Surface energy[a] (eV/atom)	CO Adsorption energy[d]	O_2 Adsorption energy[e]
Pd	3.86	0.97[b]	30	55
Au	3.81	0.85[c]	24	39

[a] Ref. [21]

[b] Converted from SI unit (J/m^2) using packing density of 1.32×10^{19} atom/m^2 for Pd(111)

[c] Converted from SI unit (J/m^2) using packing density of 1.21×10^{19} atom/m^2 for Au(111)

[d] Ref. [32]

[e] Ref. [33]

with Pd-rich surfaces. Having the fact that XPS in vacuum shows oxygen (i.e., PdO_x) on as-prepared samples in mind, we have concluded that the Pd-rich shells are kinetically stabilized by the conditions of our colloidal bimetallic nanoparticle synthesis.

4.2 Composition-Dependent and Reaction-Induced Surface Restructuring and Synergism in the Catalytic CO Oxidation Reaction

For the bimetallic Au–Pd NP system, the surface composition remains unchanged under reactive gas (i.e., CO and O_2 gases)- and/or thermally-perturbed (i.e., in vacuum at elevated temperatures) conditions with the exception of the $Au_{0.75}Pd_{0.25}$ NPs. For $Au_{25}Pd_{75}$, Pd segregates by strongly binding to CO and O_2 because of the fact that CO and O_2 have larger adsorption energies on Pd compared to that on Au (see Table 1) [32–35]. The same is true at $Au_{50}Pd_{50}$. This is actually consistent with the enrichment of Pd on AuPd(100) surface at pressures higher than 100 mTorr under CO oxidation reaction conditions [36, 37].

At $Au_{0.75}Pd_{0.25}$, Au totally covers the nanoparticle surface by forming a thin shell at 200 °C so that CO and O_2 have no access to the strongly binding Pd in the inner shells. In other words, lower surface free energy of Au-rich surfaces overcomes the energy gained by adsorbing CO and O_2 on Pd-rich surfaces (Table 1). This possibly stems from the relatively thin Pd shells in the surface regions of the $Au_{0.75}Pd_{0.25}$ NPs such that Au could easily exchange with Pd to segregate to the surface. The migration of Pd into the subsurface layers would increase the number of pair-wise Pd–Pd and Pd–Au interactions, and in turn the total cohesive energy. Additionally, the total surface free energy of the overall system would also benefit from the resulting Au-enrichment on the surface.

The catalytic evaluation of our $Au_{100-x}Pd_x$ ($x = 25$ and 75) NPs catalysts for the model CO/O_2 reaction under identical pressure and temperature conditions of the AP-XPS studies are in agreement with the picture described above. As expected from entropic considerations, the turnover rates in the mTorr regime are intrinsically lower compared to those that measured at 1 atm. For the $Au_{1-x}Pd_x$ ($x = 0$–1) NP system, 8 nm Au catalyst showed the lowest catalytic activity at 200 °C. Next to Au catalyst in activity, 9.5 nm Pd catalysts performed only slightly better than Au. The light-off behavior and the turnover rates for Pd NPs are in agreement with those reported on evaporated clusters at low pressures (ca. 10^{-5} Torr) [38]. The large particle size and gold-only catalysis explains the low turnovers in the case of Au [39, 40]. Interestingly, the general catalytic trend for the equilibrium states of our Au–Pd NP system are in favor of a synergistic effect [41], that is the Au_xPd_{1-x} ($x = 0.25$–0.75) NPs have higher catalytic activities than the parent Pd and Au NPs of comparable average sizes. Recently, Goodman and co-workers found on the single crystal AuPd(100) surfaces drastically higher activities relative to single crystal Pd and Au surfaces toward the CO/O_2 reaction under comparable temperature and pressure conditions [36, 37]. They attributed this catalytic enhancement to the CO adsorbate-induced formation of Pd contiguous sites on the surface.

5 Summary

Bimetallic Au_xPd_{1-x} nanoparticle catalysts with narrow size distributions about 10 nm were synthesized via a modified one-pot polyol reduction reaction route. The combined average bulk information from the depth-resolved XPS spectra of the nanoparticle monolayers and local information from the STEM/EDS phase mapping of multiple *single* nanoparticles allow us to clearly identify the atomic distribution and chemical composition of the bimetallic Au_xPd_{1-x} NP catalysts. Both XPS depth-profiles and STEM/EDS phase maps show that the as-synthesized Au_xPd_{1-x} ($x = 0.25$, 0.5, 0.75) nanoparticles exhibit gradient alloy (i.e., core–shell) structures with Pd-rich shells and Au-rich cores. The formation of Pd-rich shells is driven by the initial nucleation of Au and simultaneous growth of Pd. STEM/EDS spectra also show that Au core sizes increases whereas Pd shell thicknesses decrease with increasing Au concentration. The $Au_{0.25}Pd_{0.75}$ and $Au_{0.5}Pd_{0.5}$ NPs with relatively thick Pd shells are stable at 200 °C in vacuum and under various gas atmospheres (H_2, O_2, CO, etc.) and the CO/O_2 reaction conditions. Hence, they show no significant change in their surface compositions. However, the $Au_{0.75}Pd_{0.25}$ NPs restructures irreversibly to Au-rich surfaces via Au enrichment in the surface regions dominantly at 200 °C and under the CO/O_2 reaction in the Torr pressure regime. This structural behavior is also consistent with the catalytic studies of the Au_xPd_{1-x} ($x = 0$, 0.25, 0.5, 0.75, 1) NPs catalysts upon reactions at 200 °C under 80 mTorr CO and 200 mTorr O_2. Importantly, a 'synergistic effect' for the plots of turnover rates versus the surface composition was isolated: (1) all bimetallic nanoparticles showed higher turnover rates than the parent monometallic nanoparticles, and (2) the $Au_{0.25}Pd_{0.75}$ NPs showed the highest turnover rate and the $Au_{0.5}Pd_{0.5}$ NPs the lowest among all bimetallic nanoparticle catalysts studied.

Acknowledgments This work is funded by Honda Corporation and supported by the Director of the Office of Science, Office of Basic Energy Sciences of the U.S. Department of Energy under contract no. DE-AC02-05CH11231. The authors acknowledge support of the National Center for Electron Microscopy, Lawrence Berkeley Lab, which is supported by the U.S. Department of Energy under Contract

DE-AC02-05CH11231. Work at the Molecular Foundry was supported by the Director, Office of Science, Office of Basic Energy Sciences, Division of Material Sciences and Engineering, of the U.S. Department of Energy under Contract # DE-AC02-05CH11231. The Advanced Light Source is supported by the Director, Office of Science, Office of Basic Energy Sciences, of the U.S. Department of Energy under Contract No. DE-AC02-05CH11231.

References

1. Besenbacher F, Chorkendorff I, Clausen BS, Hammer B, Molenbroek AM, Norskov JK, Stensgaard I (1998) Science 279:1913–1915
2. Greeley J, Mavrikakis M (2004) Nat Mater 3:810–815
3. Bell AT (2003) Science 299:1688–1691
4. Chen MS, Kumar D, Yi CW, Goodman DW (2005) Science 310:291–293
5. Alayoglu S, Eichhorn B (2008) J Am Chem Soc 130:17479–17486
6. Alayoglu S, Nilekar AU, Mavrikakis M, Eichhorn B (2008) Nat Mater 7:333–338
7. Conant T, Karim AM, Lebarbier V, Wang Y, Girgsdies F, Schlogl R, Datye A (2008) J Catal 257:64–70
8. Park JY, Zhang Y, Grass M, Zhang T, Somorjai GA (2008) Nano Lett 8:673–677
9. Somorjai GA, Park JY (2008) Top Catal 49:126–135
10. Li BT, Kado S, Mukainakano Y, Miyazawa T, Miyao T, Naito S, Okumura K, Kunimori K, Tomishige K (2007) J Catal 245:144–155
11. Perez-Hernandez R, Galicia GM, Anaya DM, Palacios J, Angeles-Chavez C, Arenas-Alatorre J (2008) Int J Hydrogen Energy 33:4569–4576
12. Wang XM, Li N, Pfefferle LD, Haller GL (2009) Catal Today 146:160–165
13. Edwards JK, Solsona B, Landon P, Carley AF, Herzing A, Watanabe M, Kiely CJ, Hutchings GJ (2005) J Mater Chem 15:4595–4600
14. Ketchie WC, Murayama M, Davis RJ (2007) J Catal 250:264–273
15. Hou WB, Dehm NA, Scott RWJ (2008) J Catal 253:22–27
16. Sinfelt JH (1983) Bimetallic catalysts. Wiley, New york
17. Mizukoshi Y, Fujimoto T, Nagata Y, Oshima R, Maeda Y (2000) J Phys Chem B 104:6028–6032
18. Guczi L, Beck A, Horvath A, Koppany Z, Stefler G, Frey K, Sajo I, Geszti O, Bazin D, Lynch J (2003) J Mol Catal A-Chem 204:545–552
19. Harpeness R, Gedanken A (2004) Langmuir 20:3431–3434
20. Glaspell G, Fuoco L, El-Shall MS (2005) J Phys Chem B 109:17350–17355
21. Fan FR, Liu DY, Wu YF, Duan S, Xie ZX, Jiang ZY, Tian ZQ (2008) J Am Chem Soc 130:6949
22. Knecht MR, Weir MG, Frenkel AI, Crooks RM (2008) Chem Mater 20:1019–1028
23. Weir MG, Knecht MR, Frenkel AI, Crooks RM (2010) Langmuir 26:1137–1146
24. Xu J, White T, Li P, He CH, Yu JG, Yuan WK, Han YF (2010) J Am Chem Soc 132:10398–10406
25. Tao F, Grass ME, Zhang YW, Butcher DR, Aksoy F, Aloni S, Altoe V, Alayoglu S, Renzas JR, Tsung CK, Zhu ZW, Liu Z, Salmeron M, Somorjai GA (2010) J Am Chem Soc 132:8697–8703
26. Ferrer D, Torres-Castro A, Gao X, Sepulveda-Guzman S, Ortiz-Mendez U, Jose-Yacaman M (2007) Nano Lett 7:1701–1705
27. Tao F, Grass ME, Zhang YW, Butcher DR, Renzas JR, Liu Z, Chung JY, Mun BS, Salmeron M, Somorjai GA (2008) Science 322:932–934
28. Zhang YW, Grass ME, Kuhn JN, Tao F, Habas SE, Huang WY, Yang PD, Somorjai GA (2008) J Am Chem Soc 130:5868
29. Kan CX, Cai WP, Li CC, Zhang LD, Hofmeister H (2003) J Phys D Appl Phys 36:1609–1614
30. Boscoboinik JA, Plaisance C, Neurock M, Tysoe WT (2008) Phys Rev B 77:6
31. Pittaway F, Paz-Borbon LO, Johnston RL, Arslan H, Ferrando R, Mottet C, Barcaro G, Fortunelli A (2009) J Phys Chem C 113:9141–9152
32. Chesters MA, Somorjai GA (1975) Surf Sci 52:21–28
33. Eley DD, Moore PB (1981) Surf Sci 111:325–343
34. Canning NDS, Outka D, Madix RJ (1984) Surf Sci 141:240–254
35. Roudgar A, Gross A (2003) J Electroanal Chem 548:121–130
36. Gao F, Wang YL, Goodman DW (2010) J Phys Chem C 114:4036–4043
37. Gao F, Wang YL, Goodman DW (2009) J Phys Chem C 113:14993–15000
38. Ladas S, Poppa H, Boudart M (1981) Surf Sci 102:151–171
39. Widmann D, Liu Y, Schuth F, Behm RJ (2010) J Catal 276:292–305
40. Venezia AM, Liotta LF, Pantaleo G, La Parola V, Deganello G, Beck A, Koppany Z, Frey K, Horvath D, Guczi L (2003) Appl Catal A-Gen 251:359–368
41. Di W, Villa A, Porta F, Prati L, Dangsheng S (2008) J Phys Chem C 112:8617–8622